

Shear Thickening of Dense Suspensions: The Role of Friction

Vishnu Sivadasan,¹ Eric Lorenz,^{1,2} Alfons G. Hoekstra,^{1,3} and Daniel Bonn⁴

¹*Computational Science Lab, Institute for Informatics, University of Amsterdam.*

²*Electric Ant Lab B.V., Amsterdam, The Netherlands*

³*ITMO University, Saint Petersburg, Russian Federation.*

⁴*Institute of Physics, Faculty of Science, University of Amsterdam*

(Dated: November 2, 2021)

Abstract

Shear thickening of particle suspensions is caused by a transition between lubricated and frictional contacts between the particles. Using 3D numerical simulations, we study how the interparticle friction coefficient (μ_m) influences the effective macroscopic friction coefficient (μ) and hence the microstructure and rheology of dense shear thickening suspensions. We propose expressions for μ in terms of distance to jamming for varying shear stresses and μ_m values. We find μ to be rather insensitive to interparticle friction, which is perhaps surprising but agrees with recent theory and experiments.

I. INTRODUCTION

Understanding the rheological properties of shear thickening suspensions is scientifically challenging and highly relevant from the viewpoint of several applications [1–4]. The phenomenon of shear thickening [5–11] in which the viscosity increases with increasing shear rate and shear stress, is attributed to the formation of frictional contacts between the particles as suggested by computational results [12–14] and confirmed by experiments [15–19]. Shear thickening suspensions can be characterized by their macroscopic friction coefficient μ , given by $\mu = \sigma_{\text{shear}}/P$, with σ_{shear} the shear stress and P the confining pressure. Using suspensions under constant confining pressure, Boyer et al. [11] demonstrated that μ is a unique function of a viscous parameter I_v defined as $I_v = \eta_f \dot{\gamma}/P$, where η_f and $\dot{\gamma}$ are the fluid viscosity and the shear rate respectively. They observe similar $\mu(I_v)$ behavior for different materials (polystyrene, PMMA) and particle sizes. Gallier et al. [20] studied $\mu(I_v)$ rheology in simulations for $\phi < 0.45$ (ϕ being the particle volume fraction) and their simulations agree quantitatively with the experimental results. However, a more detailed analysis of μ and associated changes in the microstructure of the suspension is needed to shed further light on the behavior of the macroscopic friction coefficient μ and notably its relation with the microscopic inter-particle friction coefficient μ_m . Here, we perform 3D numerical simulations of dense shear thickening suspensions with varying inter-particle friction coefficients to study associated changes on μ . Based on recent results on constitutive relationships for shear thickening systems [21, 22], we propose analytic expressions for μ in terms of distance to jamming ($\phi_m - \phi$, where ϕ_m is the jamming volume fraction) for constant volume systems with varying pressure, shear stress and μ_m values. Using the average coordination number as a parameter, the microstructure of the particles in the system is analyzed to assess its influence on μ . Finally, simulations of non-spherical particles are performed to study the effect of non-sphericity on the behavior of the macroscopic friction coefficient.

II. METHODS

The numerical simulations were performed using the simulation framework SuSi [23]. We use the Lattice Boltzmann Method (LBM) based fluid to simulate the fluid field and Lagrangian particles as the solid phase. The fluid-particle interactions are modelled with

the Noble Torczynski Method [24]. Lubrication forces are calculated explicitly at particle gaps smaller than the LBM lattice spacing. Adaptive refinement of timesteps is performed in order to ensure numerical stability and accuracy, as the inter-particle forces diverge at small particle gaps. The contact normal force \mathbf{F}_{rep} between particles is calculated from the overlap of a contact repulsion layer [23] of specified thickness $d_c \approx 0.001R$ [12], where R is the mean radius of particles.

$$\mathbf{F}_{\text{rep}} = \begin{cases} -c_0 \frac{(d - d_c)^2}{dd_c^2} \mathbf{e}_h, & d \leq d_c \\ 0 & \text{otherwise} \end{cases} \quad (1)$$

where c_0 is the repulsion coefficient, d is the gap between the particles, d_c is the repulsion layer thickness and \mathbf{e}_h is the connecting unit vector between the particles. The static and kinetic friction between particles is modeled as proposed by Luding [25]. Upon initiation of frictional contact between particle pairs, a linear spring of length ξ is initialized between the closest surface points to model static friction and is updated using the relative tangential velocity between the two contacting surface points. The maximum static friction is $F_s \leq \mu_s |\mathbf{F}_{\text{norm,fric}}|$, as given by Coulomb's Law. The spring force \mathbf{F}_{spr} is applied if the amplitude of $\mathbf{F}_{\text{spr}} = -k\xi$ is smaller than the maximum possible static friction force F_s . Kinetic friction $F_k = \mu_k |\mathbf{F}_{\text{norm,fric}}|$ is applied as a tangential force at the surface points if F_{spr} exceeds F_s . For kinetic friction, the static friction spring length is rescaled so that $F_{\text{spr}} = F_k$. In our simulations, we keep $\mu_s = \mu_k = \mu_m$, where μ_m is referred to as the microscopic friction coefficient.

The interacting particles are deemed frictional based on a Critical Load Model [12], where two particles are considered to be in friction if the normal force (F_{rep}) between the contacting particles exceeds a threshold value (F_{CL}). The static and kinetic friction is based on the normal force for friction ($F_{\text{norm,fric}}$), calculated as [12]:

$$F_{\text{norm,fric}} = \begin{cases} |\mathbf{F}_{\text{rep}}| - F_{\text{CL}} & \text{if } |\mathbf{F}_{\text{rep}}| \geq F_{\text{CL}}, \\ 0 & \text{otherwise.} \end{cases} \quad (2)$$

For the simulations discussed in the subsequent sections, a $96\mu\text{m} \times 64\mu\text{m} \times 96\mu\text{m}$ system is used, which contains ≈ 650 particles for $\phi = 0.56$. The particles are have a mean diameter of $8\mu\text{m}$ with a standard deviation of $0.4\mu\text{m}$ to avoid crystallization. The particles are neutrally buoyant in the suspending fluid, which mimics water (fluid viscosity $\eta_f = 1.002 \times 10^{-3} \text{Pa}\cdot\text{s}$, density $\rho_f = 1000 \text{kg}/\text{m}^3$). The simulated systems have a characteristic stress for frictional

contacts, given by $\sigma_0 = F_{\text{CL}}/(6\pi R^2)$, where R is the average particle radius. For the performed analysis, we choose instances of the system with average shear stress greater than σ_0 , so that frictional interactions are significant.

III. RESULTS AND DISCUSSION

The macroscopic friction coefficient (μ) of suspensions is characterized by the viscous number (I_v) of the suspension flow. I_v is defined as $I_v = \eta_f \dot{\gamma}/P$, where η_f is the fluid viscosity, $\dot{\gamma}$ is the shear rate and P is the pressure in the system. The viscous number can be seen as the ratio of the internal timescale of microscopic particle rearrangements in a viscous system (η_f/P), to the macroscopic flow timescale ($1/\dot{\gamma}$). Boyer et al. [11] used pressure imposed flows to study variation in μ with I_v , where systems of hard spheres were sheared at constant pressure (P) and shear rate ($\dot{\gamma}$) while the system was allowed to dilate (changing ϕ) in order to keep P constant. They demonstrated that μ of suspensions is the sum of contact (μ_c) and hydrodynamic (μ_h) stress contributions, as shown in Eq.3.

$$\mu(I_v) = \underbrace{\mu_1 + \frac{\mu_2 - \mu_1}{1 + I_0/I_v}}_{\mu_c} + \underbrace{I_v + \frac{5}{2}\phi_m I_v^{\frac{1}{2}}}_{\mu_h} \quad (3)$$

Where, μ_1 is the limit of of the particle contact contribution to macroscopic friction (μ_c) at vanishing viscous numbers, and μ_2 is the maximum μ_c at $I_v \rightarrow \infty$ as observed in granular flows [26, 27]. I_0 represents the scale over which $\mu_c(I_v)$ changes and is observed to be constant for a given particle shape. ϕ_m is the jamming volume fraction. $\mu_h(I_v)$ is designed to reproduce the Einstein viscosity at low ϕ and be non-saturating at high I_v . Here, simulations of constant ϕ and $\dot{\gamma}$ with varying P are performed to study $\mu(I_v)$. In this study, we define P as the average of the diagonal elements of the stress tensor in the system i.e. $P = \sum_{i=1}^3 \sigma_{ii}/3$. We systematically vary the microscopic friction coefficient μ_m and compare to the predictions of $\mu(I_v)$ rheology (Eq. (3)), to see if the constant ϕ and $\dot{\gamma}$ simulations conform to the predictions of $\mu(I_v)$ rheology.

Fig.1(a) compares the the results from our simulations to the $\mu(I_v)$ rheology predicted by Eq.3, and the experimental results from Boyer et al. [11]. Suspensions of different ϕ values were simulated to obtain the range of I_v values. It can be observed that $\mu \approx 0.34$ at vanishing I_v , which is similar to the values obtained in experiments [11, 26]. Using $\mu_2 = 0.7$

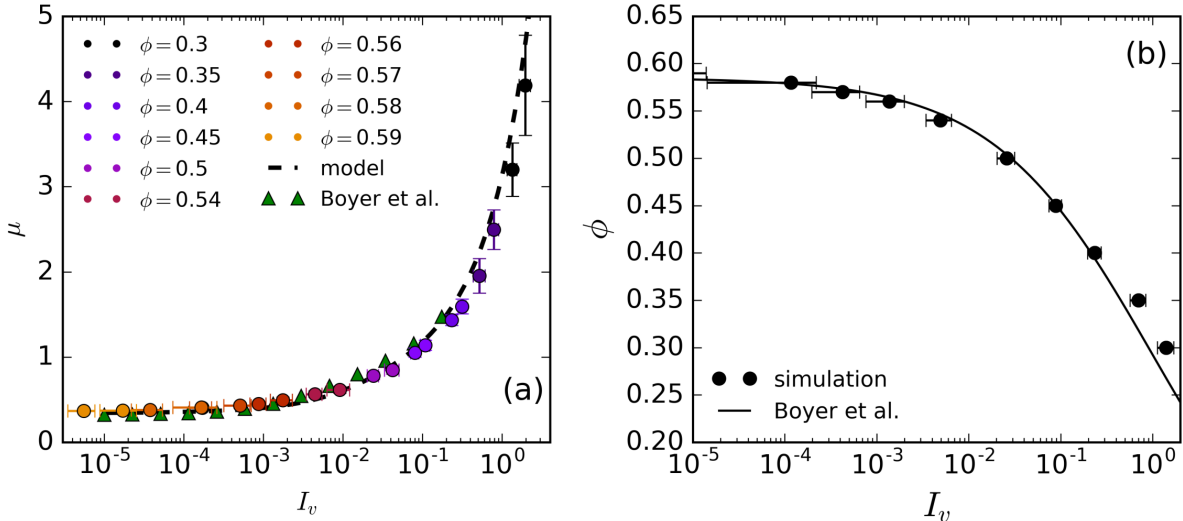


FIG. 1. **(a)** Macroscopic friction coefficient μ vs viscous number I_v comparison between simulation and model. Dots represents μ prediction from simulations of ϕ corresponding to its color. The dashed line shows the $\mu(I_v)$ prediction from Eq. (3) with $\mu_1 = 0.34$ (minimum μ observed), $\mu_2 = 0.7$ and $I_0 = 0.009$ providing a good fit to the simulation results. The microscopic friction coefficient $\mu_m = 0.5$. Triangles represent the experimental results from Boyer et al. [11]. Vertical and horizontal errorbars correspond to variation in μ and I_v in the data, in each I_v interval. **(b)** Variation in ϕ vs viscous number I_v . Dots represent simulation results, and the line represents results from Boyer et al. [11]. Error bars represent the range of I_v values observed for a given ϕ .

and $I_0 \approx 0.009$ provides a good fit to the simulation data. The value for μ_2 is the same as that observed previously in experiments and simulations of spherical particles [11, 20].

At vanishing I_v , we find high corresponding ϕ values similar to that in experiments [11]. Under constant ϕ settings, the range of I_v values accessible for each ϕ value is limited (as seen in Fig. 1(b)), and multiple simulations of varying ϕ values are required to capture I_v values varying in orders of magnitude. This issue can be overcome by allowing the system to dilate in order to change ϕ , as done in experiments. The variation in ϕ with I_v is shown in Fig. 1(b), along with the experimental observation from Boyer et al. [11]. The simulations show good agreement with the experimental results.

A. Effect of varying microscopic friction coefficient

Earlier simulation studies of the role of the microscopic friction coefficient (μ_m) were performed at large viscous numbers ($I_v > 0.1$) with limited overlap between I_v ranges studied in experiments [20]. Here, a larger range of I_v values is accessed, allowing comparisons with experimental results at lower I_v values. In order to study the effect of changing μ_m on μ , simulations of $0.01 \leq \mu_m \leq 10$ are performed, while keeping all other system parameters the same. This amounts to over 500 individual simulations, the results of which are presented in Fig. 2.

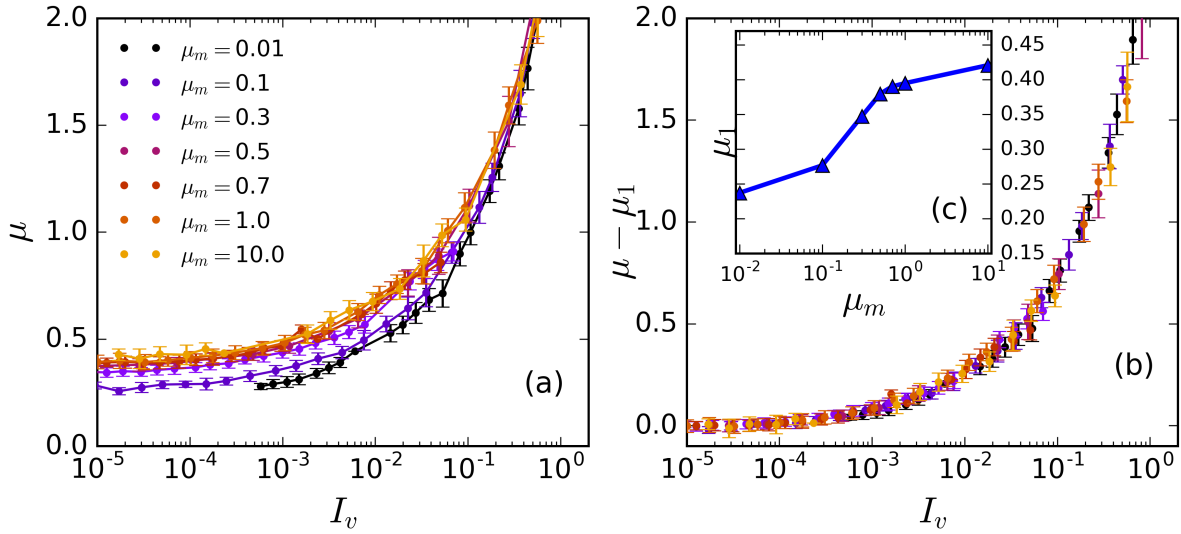


FIG. 2. (a) Macroscopic friction coefficient μ vs viscous number I_v for different microscopic friction coefficients (μ_m). Each dot represents the prediction from simulations of corresponding μ_m value. Results are compiled over various ϕ and $\dot{\gamma}$ values for each μ_m value in consideration. (b) $\mu - \mu_1$ vs I_v where μ_1 is the minimum μ observed. (c) Change in the minimum μ observed (i.e. μ_1) with μ_m .

In Fig. 2(a) the simulation results of $\mu(I_v)$ for various μ_m values are shown. At large I_v values ($I_v > 0.1$), $\mu(I_v)$ is similar for all μ_m values. At vanishing I_v values ($I_v < 10^{-4}$), the minimum $\mu(I_v)$ (i.e. μ_1) reduces with decreasing μ_m , as shown in Fig. 2(c). This observation is in agreement to that made in past simulations of 2D granular and suspension flows [28, 29]. Interestingly, the relationship between $\mu - \mu_1$ and I_v collapses to the same curve for all μ_m values in this system (see Fig. 2(b)). Such a collapse was not observed when

spherical particle suspensions studied in this section are compared against non-spherical particle suspensions (see Section III D), suggesting that particle shape is a factor here. The change in μ_1 with μ_m follows a sigmoidal relationship, as observed in Fig. 2(c). The collapse of $\mu - \mu_1$ for $I_v < 10^{-3}$ with the viscous number is obviously due to μ being constant and equal to μ_1 in this range. Within the intermediate viscous number range ($10^{-3} \leq I_v \leq 10^{-1}$) where the particle contact contribution (μ_c in Eq. (3)) to μ is dominant, the variation in μ with the microscopic friction coefficient μ_m is dictated by the variation in $\mu_2 - \mu_1$ with μ_m . Seeing that μ_2 is rather insensitive to microscopic inter-particle friction coefficients (μ_2 varies between 0.7 and 0.8 for completely frictionless and frictional particles respectively [20]), we estimate that the largest difference in $\mu - \mu_1$ between systems of $\mu_m = 0.01$ and $\mu_m = 10.0$ should be ≈ 0.2 , which agrees with the observed variations in $\mu - \mu_1$ with μ_m at $I_v \approx 10^{-1}$. For large viscous number range ($I_v > 10^{-1}$), the variations in μ are dominated by the hydrodynamic component (μ_h in Eq. (3)), and does not depend on the friction.

The main contribution to $\mu - \mu_1$ is therefore given by the distance to jamming. The collapse of the data for $\mu - \mu_1$ as a function of I_v for $0.01 \leq \mu_m \leq 10$ implies that at the same microscopic to macroscopic particle rearrangement timescale ratios (i.e. I_v), all systems will have the same distance to jamming, regardless of their microscopic friction coefficient. This also entails that if $\mu - \mu_1$ indeed is a measure of the distance of a system from jamming, it should have a mapping to some other measure of distance to jamming, such as $\phi_m - \phi$. We shall explore this in the following section.

B. Macroscopic friction coefficient and distance to jamming

In the simulations, a range of shear stresses (σ_{shear}), volume fractions (ϕ) and microscopic friction coefficients (μ_m) are studied. From previous experiments and simulations [21, 22], we understand the effect of changing each of these parameters on the rheology, especially on the jamming volume fraction (ϕ_m). Shear thickening is due to the formation of system spanning frictional networks, and the best way to describe this is to look at the fraction of frictional particles in the system. Beyond a characteristic shear stress σ_0 , the fraction of particles in the system that have frictional contacts (f) increases until all particles become

frictional [12]. This increase in f with shear stress σ_{shear} can be described [30] as

$$\sigma_0 = F_{\text{CL}}/6\pi R^2 \quad (4)$$

$$\tilde{\sigma} = \sigma_{\text{shear}}/\sigma_0 \quad (5)$$

$$f = e^{(-1.45/\tilde{\sigma})} \quad (6)$$

where R is the average radius of the particles, F_{CL} is the onset normal force between particles to initiate friction, and $\sigma_0 = F_{\text{CL}}/(6\pi R^2)$ is the characteristic stress for the onset of friction. Increasing the fraction of frictional particles leads to a lower jamming volume fraction ϕ_m , as ϕ_m for frictional particles is lower than non frictional particles [21, 22]. This is a result of the frictional particles requiring a smaller number of inter-particle contacts to be arrested in comparison with frictionless particles [31]. The average coordination number for jamming (Z_J) in suspensions varies continuously between $Z_J(\mu_m = \infty) = 4$ and $Z_J(\mu_m = 0) = 6$ in suspensions. Increasing the fraction of frictional particles in the system reduces the jamming volume fraction ϕ_m from that of a lubricated, non-frictional suspension (ϕ_J^0) to that of a frictional suspension (ϕ_J). $\phi_J(\mu_m)$ is the jamming volume fraction in a suspension with all particles in frictional contact and is a decreasing function of the microscopic friction coefficient μ_m . Hence, the volume fraction associated with jamming varies with μ_m and the fraction of frictional particles f in the system, and can be described [21] by

$$\phi_m(\tilde{\sigma}, \mu_m) = \phi_J(\mu_m)f(\tilde{\sigma}) + \phi_J^0(1 - f(\tilde{\sigma})) \quad (7)$$

where $\phi_J(\mu_m)$ represents the jamming volume fraction when $f = 1$ for a given microscopic friction coefficient μ_m . ϕ_J^0 is the jamming volume fraction when $f = 0$, which is equivalent to a $\mu_m = 0$ (frictionless) state. Changing the microscopic friction coefficient μ_m influences ϕ_m , as lowering μ_m increases ϕ_J , according to Eq. (8) [21]

$$\phi_J(\mu_m) = \phi_J^0 - (\phi_J^0 - \phi_J^\infty)e^{-\mu_\phi/\mu_m} \quad (8)$$

Here, ϕ_J^∞ is the jamming volume fraction at large μ_m values, and μ_ϕ is a constant. Boyer et al. [11] proposed a model for I_v in terms of ϕ_m and ϕ as:

$$\phi(I_v) = \frac{\phi_m}{1 + I_v^{0.5}} \quad (9)$$

when substituted in Eq. (3), this gives μ as a function of ϕ_m and ϕ :

$$\mu(\phi, \phi_m) = \underbrace{\mu_1 + \frac{\mu_2 - \mu_1}{1 + I_0\phi^2/(\phi_m - \phi)^2}}_{\mu_c} + \underbrace{\left(\frac{\phi_m - \phi}{\phi}\right)^2 + \frac{5}{2}\frac{\phi_m}{\phi}(\phi_m - \phi)}_{\mu_h} \quad (10)$$

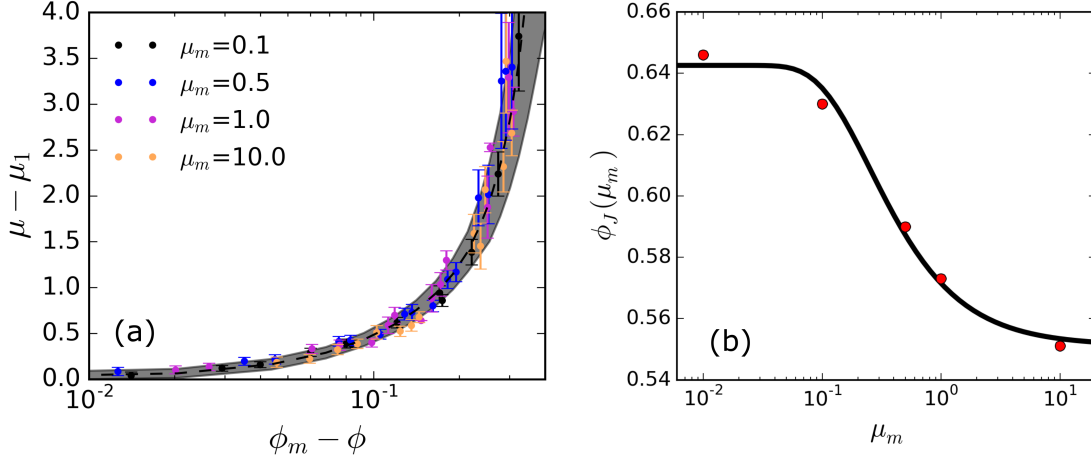


FIG. 3. **(a)** Macroscopic friction coefficient $\mu(\phi, \sigma_{\text{shear}}, \mu_m) - \mu_1(\mu_m)$ vs distance to jamming $\phi_m - \phi$ for different μ_m , σ_{shear} , and ϕ values. Shaded area represents the range of values of $\mu - \mu_1$ predicted by Eq. (10), correcting for changes in ϕ_m according to Eqs. (4) to (8), and the dashed line represents their mean. μ_1 values are as given by Fig. 2(b), $\mu_2 = 0.7$. **(b)** Frictional jamming volume fraction $\phi_J(\mu_s)$ for different microscopic friction coefficient (μ_m) values. Red dots represent the simulation data, while the curve represents the model presented in Eq. (8) with $\phi_J^0 = 0.643$, $\phi_J^\infty = 0.55$ and $\mu^\phi = 0.25$.

Under constant volume settings, the fraction of the frictional contacts varies with shear stress (or shear rate) in the system, which in turn varies ϕ_m . We can account for this variation in ϕ_m by employing Eqs. (4) to (8). This helps to predict ϕ_m in our constant volume system in terms of σ_{shear} and μ_m which in turn enables an analysis of μ as a function of $\phi_m - \phi$ (i.e. a distance to jamming metric) and compare against the predictions from Eq. (10).

Fig. 3(a) shows the $\mu - \mu_1$ as a function of $\phi_m - \phi$ compiled over a range of σ_{shear} , ϕ and μ values. The simulation results show agreement with the predictions from theory outlined in Eqs. (4) to (10). The changes in ϕ_J with μ_m are taken into account by using their relationship outlined in Eq. (8), as shown in Fig. 3(b). The simulation results agree with the theoretical assumption that, by accounting for changes in ϕ_m with σ_{shear} and μ_m , the values of μ across different σ_{shear} and μ_m values collapse to the regime outlined in Fig. 3(a). The change in the frictional jamming volume fraction ϕ_J with μ_m is shown in Fig. 3(b), along with the model presented in Eq. (8). The results also show that $\mu - \mu_1$ is indeed a measure for the distance to jamming, as suggested in the previous section.

C. Microstructure changes

The microscopic friction coefficient plays an important role in the nature of contact networks formed at jamming. The mean coordination number at which the suspension jams (Z_J), is inversely dependent on μ_m , as $Z_J(\mu_m = 0) = 6$ and $Z_J(\mu_m = \infty) = 4$ [31]. The evolution of μ with average coordination number (Z) under varying μ_m values thus, is of interest. It is also compelling to view $\mu(I_v)$ rheology in terms of the evolution of Z .

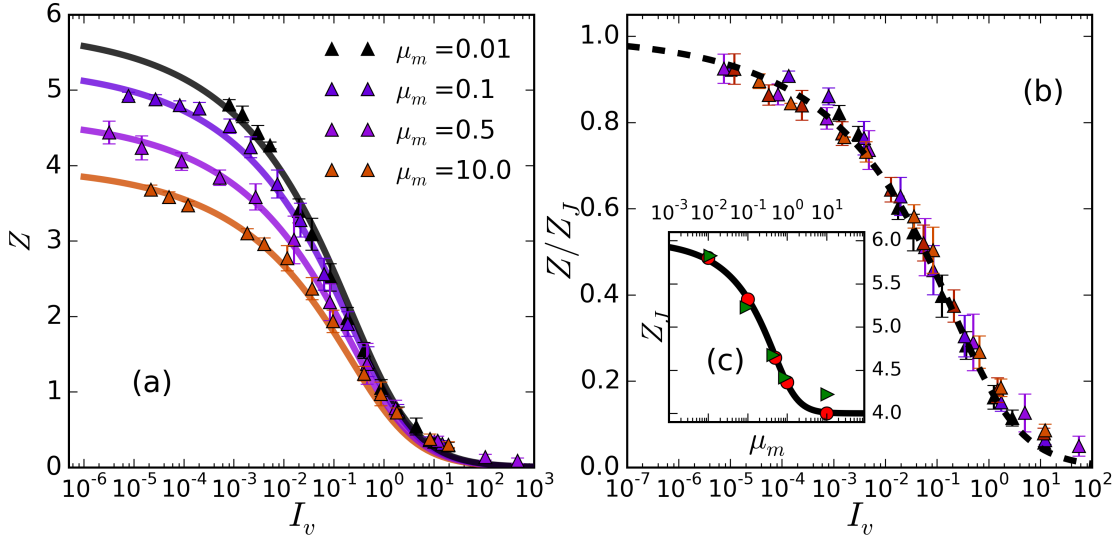


FIG. 4. (a) Average coordination number Z as a function of viscous number I_v for different μ_m compiled across different ϕ and σ_{shear} values. Each dot corresponds to simulation results at corresponding μ_m . Lines show the prediction of $Z(I_v)$ from Eqs. (11) and (12). (b) Z normalized by jamming coordination number Z_J vs I_v . The dashed line represents the $Z/Z_J(I_v)$ model from Eq. (11) while dots represent the simulation results of μ_m . (c) Variation in Z_j with μ_m . The dots show Z_J as observed in simulations at vanishing I_v . The line represents the $Z_J(\mu_m)$ model from Eq. (12). Green triangles represent the random loose packing limits in simulations of granular system [31].

Fig. 4(a) shows average coordination number $Z(I_v)$ under various μ_m values. Z is calculated per particle by counting the number contacts it makes, i.e. cases where $r_{ij} - R_i - R_j \leq d_c$ where $r_{i,j}$ are the distance between the particles and $R_{i,j}$ are their radii. Even though the data is compiled from various ϕ and σ_{shear} values, $Z(I_v, \mu_m)$ collapses to unique curves depending on μ_m . The maximum coordination number is $Z \approx 4$ at $\mu_m = 10.0$ and saturates

at higher maximum values (Z_J) with reducing μ_m as expected from $Z_J(\mu_m)$ relationship described before. The low Z values at large I_v sheds light on the the insensitivity of $\mu(I_v)$ rheology to changes in μ_m in these I_v ranges. $\mu(I_v)$ rheology hence is essentially the process of varying coordination numbers between zero and $Z_J(\mu_m)$. Upon normalizing Z by $Z_J(\mu_m)$, the different $Z(\mu_m)$ curves collapse to a single curve, which can be modeled as:

$$\frac{Z}{Z_J} = 1 - (1 + I_v^{\alpha_1})^{-\beta_1} \quad (11)$$

where $\alpha_1 = 0.77$ and $\beta_1 = 0.3$. The variation in Z_J between 6 and 4 depending on μ_m can also be modeled using the expression:

$$Z_J = 6 - 2(1 + \mu_m^{\alpha_2})^{-\beta_2} \quad (12)$$

where $\alpha_2 = -1.72$ and $\beta_2 = 0.27$. Fig. 4(b) shows Z/Z_J as a function of I_v , and it can be observed that the data collapses to a single curve, modeled by Eq. (11). The variation in Z_J with μ_m , modeled by Eq. (12) is shown in Fig. 4(c). It is relevant to note that the variation in Z_J with μ_m is found to be quite similar to the change in the coordination numbers associated with minimum random loose packing (RLP) limit observed in dry granular systems [31]. The minimum RLP coordination number corresponds to the minimum coordination number required to obtain a disordered, mechanically stable jammed system. As the limits of jamming are prescribed entirely by the properties of the particles, it is conceivable that the characteristics related to jamming in granular systems devoid of fluid is to be expected in suspensions as well.

The effect of changing Z on μ , under various μ_m values is shown in Fig. 5(a). $\mu(Z)$ values reasonably collapses into a single curve for all values of μ_m studied. This demonstrates that the the minimum μ achieved at low I_v values (i.e. μ_1) is determined by Z_J . As Z_J is inversely related to μ_m , the relationship between μ_1 and μ_m depicted in Fig. 2(b) can be rationalized. Assuming a range of I_v values, one can calculate and compare μ against Z for a given μ_m value using the relationships outlined in Eqs. (3), (8), (11) and (12). As shown in Fig. 5(a), the theoretical predictions of $\mu(Z, \mu_m = 0.5)$ is in agreement with the simulation results. Consequently, the variation in μ with ϕ also collapses reasonably onto a simple curve across the various μ_m values studied, as seen in Fig. 5(b). This behavior is observed in 2D simulations of sheared suspensions and dense granular systems [28, 32] and experimentally by Boyer et al.[11]. With increasing volume fraction, under a given shear rate, the shear

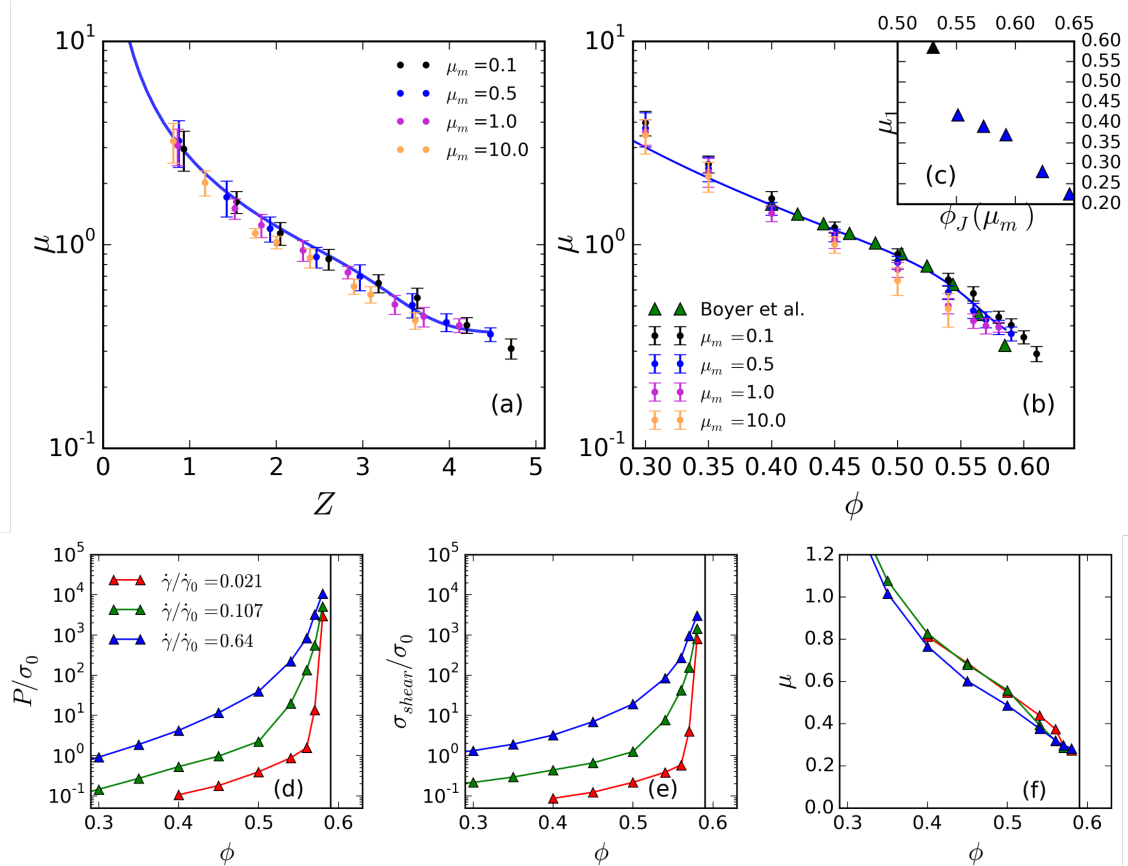


FIG. 5. **(a)** Variation in the macroscopic friction coefficient μ with average coordination number Z compiled across different μ_m and ϕ values. Solid line represents the theoretical prediction of $\mu(Z)$ for $\mu_m = 0.5$. **(b)** Variation of μ with ϕ for various μ_m values. Solid line represents the theoretical prediction of $\mu(\phi)$ for $\mu_m = 0.5$. Green triangles represent the experimental results from Boyer et al. [11]. **(c)** Minimum macroscopic friction coefficient (μ_1) achieved at jamming as a function of the jamming volume fraction $\phi_J(\mu_m)$. Black triangle represents the μ_1 observed at jamming for suspensions of non-spherical particles discussed in Section III D. **(d,e)** Pressure P and shear stress σ_{shear} normalized by σ_0 scaling with volume fraction for various shear rates for $\mu_m = 0.5$. **(f)** Macroscopic friction coefficient μ measured for the pressure and shear stresses shown in **(d,e)**. Vertical black lines show the jamming volume fraction.

stress and normal stresses become larger, but their ratio (μ) reduces till $\mu = \mu_1$ at jamming (see Fig. 5(d-f)).

This implies that the jamming volume fraction determines μ_1 , the minimum macroscopic friction coefficient. The lower the jamming volume fraction, the higher the observed μ_1 ; see

Fig. 5(c). Our simulations of non-spherical particle suspensions (see next section) that jam at a lower volume fraction compared to spherical particles also agree with this observation, as shown in Fig. 5(c).

D. Non spherical particles

Particle shapes have significant effects on the shear thickening behavior of the suspensions. Cornstarch particles are observed to shear thicken at much lower ϕ_m values ($\phi_m \approx 0.44$) [6] in comparison to suspensions of spherical particles which shear thicken around $\phi_m = 0.56$. Simulation results [23] show that frictional jamming volume fraction ϕ_J^∞ is lowered when particles shapes become 'cornstarch-like'. In the interest of comparing the macroscopic friction coefficient variation in spherical particles to that of non-spherical particles, simulations of 'cornstarch-like' non-spherical particle suspensions were performed. The 'cornstarch-like' particles were created using overlapping spheres of varying sizes, as outlined in [23]. A representation of the non-spherical particles used is provided in Fig. 6(a)(inset).

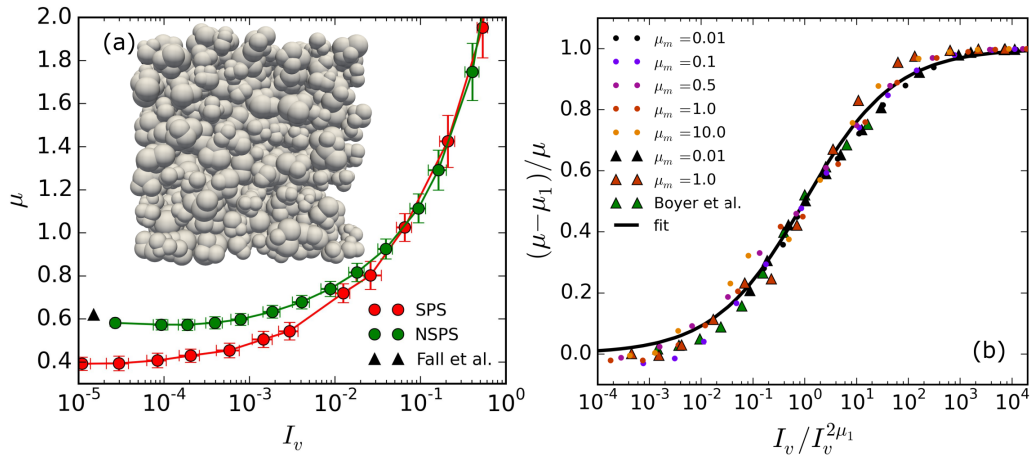


FIG. 6. **(a)** Macroscopic friction coefficient μ vs viscous number I_v for spherical particle suspensions (SPS) and non spherical particle suspensions (NSPS) with $\mu_m = 1.0$. Black triangle represent the macroscopic friction coefficient measured close to jamming in experiments with cornstarch suspensions [6]. **(inset)**: Representation of the non-spherical particles used in the simulations. **(b)** $(\mu - \mu_1)/\mu$ for spherical (dots) and non-spherical (triangles) particle suspensions. Green triangles represent the results of Boyer et al.[11]. Line represents the fit given by Eq. (13).

Fig. 6(a) compares $\mu(I_v)$ for spherical particle suspensions and non-spherical particle suspensions. At high viscous numbers, $\mu(I_v)$ for spherical and non-spherical particle suspensions tends to be the same. This is understandable, as at high I_v values the coordination numbers of the particles (spherical or non-spherical) in the suspensions reduces and particle shapes become increasingly less relevant. However, at small I_v values, $\mu(I_v)$ behavior of non-spherical particle suspensions deviates from that of spherical particle suspensions, for any constant μ_m value. Naturally, these deviations become apparent at I_v values where particle interactions become relevant, i.e. $I_v < 10^{-1}$. Results suggests that the macroscopic friction coefficient of non-spherical particle suspensions plateaus to μ_1 at higher viscous numbers in comparison to the spherical particle suspensions. Also, at vanishing viscous numbers, the macroscopic friction coefficient of the non-spherical particle suspensions saturates to a higher μ_1 in comparison with spherical particle suspensions, for a given μ_m value. This agrees with measurements of the macroscopic friction coefficient for cornstarch suspensions close to jamming [6], where $\mu_1 \approx 0.62$ in the experimental systems and $\mu_1 \approx 0.6$ in the simulations. In the previous section, it was concluded that the jamming volume fraction determines the minimum value of the macroscopic friction coefficient. Considering that the non-spherical suspension simulated here jams around $\phi_J^{non-spherical} = 0.53$, which is lower than the jamming volume fraction for spherical particles ($\phi_J^{spherical} = 0.576$) at the same μ_m value ($\mu_m = 1$), the larger μ_1 observed here can be rationalized.

It is intriguing to see whether one can generalize these variations in μ with particle shapes and microscopic friction coefficients to arrive at a common curve for all available data. By (a) normalizing I_v with $I_v^{2\mu_1}$ (where $I_v^{2\mu_1} = I_v(\mu = 2\mu_1)$) to account for the shift in I_v values at which μ plateaus to μ_1 , and (b) setting upper and lower bounds to the variation in μ by using $(\mu - \mu_1)/\mu$ as the measure of the variation of μ with I_v , the results collapses nicely to a single curve, for both spherical and non-spherical particle suspensions, across varying μ_m values (see Fig. 6(b)). The results of Boyer et al. [11] are shown for comparison, and also agrees with the curve. This common relationship can be fitted using the curve given by:

$$\frac{\mu - \mu_1}{\mu} = \frac{\sqrt{I_v}}{\sqrt{I_v} + \sqrt{I_v^{2\mu_1}}} \quad (13)$$

which in turn gives:

$$\mu = \mu_1 \left(1 + \sqrt{\frac{I_v}{I_v^{2\mu_1}}} \right) \quad (14)$$

Even though the simulation results conform to the expression given by Eq. (13), it should be mentioned that the validity of the expression at high viscous numbers ($I_v > 0.5$) is suspect, as we have no experimental data in this regime. Experimental data for non-spherical particles at viscous numbers high enough to obtain $I_v^{2\mu_1}$ is also absent, which prevents us from further validation.

IV. CONCLUSION

We analyze the behavior of the macroscopic friction coefficient (μ) under different microscopic friction coefficients (μ_m) using 3D numerical simulations. The predictions of μ from simulations agree with earlier predictions of viscous number granular suspension rheology. We find that when $\mu_m > 0.3$, that viscous number rheology is largely insensitive to the value of μ_m . By changing the jamming volume fraction ϕ_m with the changes in shear stresses and μ_m , we analyze μ in terms of distance to jamming ($\phi_m - \phi$) and provide phenomenological but analytic formulae that match the observations. Our results also suggest the behavior of μ across various μ_m and viscous numbers (I_v) can be reduced to effects of distance to jamming. The study of changes in the average coordination number (Z) with viscous number (I_v) shows that Z smoothly decreases from Z_J (Z at jamming) to zero with increasing viscous number, where Z_J is again determined by μ_m . Our results suggest that the minimum μ achieved is inversely related to the jamming volume fraction and Z_J . Finally, we show that with appropriate scaling, a common curve for the variation of μ with I_v emerges for both spherical and non-spherical particles under varying μ_m values.

CONFLICTS OF INTEREST

There are no conflicts of interests.

ACKNOWLEDGEMENTS

We would like to thank SURFsara for using their HPC infrastructure and for providing support (project number 00231267). Author VS acknowledges funding by NWO, Nether-

lands under the CSER program (project number 14CSER026).

- [1] Young S Lee, Eric D Wetzels, and Norman J Wagner, “The ballistic impact characteristics of kevlar® woven fabrics impregnated with a colloidal shear thickening fluid,” *Journal of materials science* **38**, 2825–2833 (2003).
- [2] Min Li, Binghai Lyu, Julong Yuan, Chenchen Dong, and Weitao Dai, “Shear-thickening polishing method,” *International Journal of Machine Tools and Manufacture* **94**, 88–99 (2015).
- [3] MJ Decker, CJ Halbach, CH Nam, NJ Wagner, and ED Wetzels, “Stab resistance of shear thickening fluid (stf)-treated fabrics,” *Composites science and technology* **67**, 565–578 (2007).
- [4] Colin D Cwalina, Charles M McCutcheon, Richard D Dombrowski, and Norman J Wagner, “Engineering enhanced cut and puncture resistance into the thermal micrometeoroid garment (tmg) using shear thickening fluid (stf)–armor absorber layers,” *Composites Science and Technology* **131**, 61–66 (2016).
- [5] Morton M Denn, Jeffrey F Morris, and Daniel Bonn, “Shear thickening in concentrated suspensions of smooth spheres in newtonian suspending fluids,” *Soft matter* **14**, 170–184 (2018).
- [6] Abdoulaye Fall, François Bertrand, Guillaume Ovarlez, and Daniel Bonn, “Shear thickening of cornstarch suspensions,” *Journal of rheology* **56**, 575–591 (2012).
- [7] Abdoulaye Fall, François Bertrand, David Hautemayou, Cédric Mézière, Pascal Moucheron, Anael Lemaitre, and Guillaume Ovarlez, “Macroscopic discontinuous shear thickening versus local shear jamming in cornstarch,” *Physical review letters* **114**, 098301 (2015).
- [8] Eric Brown and Heinrich M Jaeger, “Shear thickening in concentrated suspensions: phenomenology, mechanisms and relations to jamming,” *Reports on Progress in Physics* **77**, 046602 (2014).
- [9] Morton M Denn and Jeffrey F Morris, “Rheology of non-brownian suspensions,” *Annual review of chemical and biomolecular engineering* **5**, 203–228 (2014).
- [10] Colin D Cwalina and Norman J Wagner, “Material properties of the shear-thickened state in concentrated near hard-sphere colloidal dispersions,” *Journal of Rheology* **58**, 949–967 (2014).
- [11] François Boyer, Élisabeth Guazzelli, and Olivier Pouliquen, “Unifying suspension and granular rheology,” *Physical Review Letters* **107**, 188301 (2011).

- [12] Romain Mari, Ryohei Seto, Jeffrey F Morris, and Morton M Denn, “Shear thickening, frictionless and frictional rheologies in non-brownian suspensions,” *Journal of Rheology* **58**, 1693–1724 (2014).
- [13] Ryohei Seto, Romain Mari, Jeffrey F Morris, and Morton M Denn, “Discontinuous shear thickening of frictional hard-sphere suspensions,” *Physical review letters* **111**, 218301 (2013).
- [14] Christopher Ness and Jin Sun, “Shear thickening regimes of dense non-Brownian suspensions,” *Soft Matter* **12**, 914–924 (2015).
- [15] Jean Comtet, Guillaume Chatté, Antoine Niguès, Lydéric Bocquet, Alessandro Siria, and Annie Colin, “Pairwise frictional profile between particles determines discontinuous shear thickening transition in non-colloidal suspensions,” *Nature communications* **8**, 15633 (2017).
- [16] Neil Y C Lin, Ben M Guy, Michiel Hermes, Chris Ness, Jin Sun, Wilson C K Poon, and Itai Cohen, “Hydrodynamic and contact contributions to continuous shear thickening in colloidal suspensions,” *Physical review letters* **115**, 228304 (2015).
- [17] Zhongcheng Pan, Henri de Cagny, Bart Weber, and Daniel Bonn, “S-shaped flow curves of shear thickening suspensions: Direct observation of frictional rheology,” *Physical Review E* **92**, 032202 (2015).
- [18] John R Royer, Daniel L Blair, and Steven D Hudson, “Rheological signature of frictional interactions in shear thickening suspensions,” *Physical review letters* **116**, 188301 (2016).
- [19] N Huang, G Ovarlez, F Bertrand, S Rodts, P Coussot, and Daniel Bonn, “Flow of wet granular materials,” *Physical review letters* **94**, 028301 (2005).
- [20] Stany Gallier, Elisabeth Lemaire, François Peters, and Laurent Lobry, “Rheology of sheared suspensions of rough frictional particles,” *Journal of Fluid Mechanics* **757**, 514–549 (2014).
- [21] Abhinendra Singh, Romain Mari, Morton M Denn, and Jeffrey F Morris, “A constitutive model for simple shear of dense frictional suspensions,” *Journal of Rheology* **62**, 457–468 (2018).
- [22] Matthieu Wyart and M E Cates, “Discontinuous shear thickening without inertia in dense non-brownian suspensions,” *Physical review letters* **112**, 098302 (2014).
- [23] Eric Lorenz, Vishnu Sivadasan, Daniel Bonn, and Alfons G Hoekstra, “Combined lattice-boltzmann and rigid-body method for simulations of shear-thickening dense suspensions of hard particles,” *Computers & Fluids* (2018), <https://doi.org/10.1016/j.compfluid.2018.03.056>.

- [24] DR Noble and JR Torczynski, “A lattice-boltzmann method for partially saturated computational cells,” *International Journal of Modern Physics C* **9**, 1189–1201 (1998).
- [25] Stefan Luding, “Cohesive, frictional powders: Contact models for tension,” *Granular Matter* **10**, 235–246 (2008).
- [26] C Cassar, M Nicolas, and O Pouliquen, “Submarine granular flows down inclined planes,” *Physics of fluids* **17**, 103301 (2005).
- [27] Pierre Jop, “Rheological properties of dense granular flows,” *Comptes rendus physique* **16**, 62–72 (2015).
- [28] Frédéric Da Cruz, Sacha Emam, Michaël Prochnow, Jean-Noël Roux, and François Chevoir, “Rheophysics of dense granular materials: Discrete simulation of plane shear flows,” *Physical Review E* **72**, 021309 (2005).
- [29] M Trulsson, E DeGiuli, and M Wyart, “Effect of friction on dense suspension flows of hard particles,” *Physical Review E* **95**, 012605 (2017).
- [30] Abhinendra Singh, Jeffrey F Morris, and Morton M Denn, “Microstructural description of shear-thickening suspensions,” *EPJ Web of Conferences* **140**, 09023 (2017).
- [31] Chaoming Song, Ping Wang, and Hernán A Makse, “A phase diagram for jammed matter,” *Nature* **453**, 629 (2008).
- [32] Jetin E Thomas, Kabir Ramola, Abhinendra Singh, Romain Mari, Jeffrey Morris, and Bulbul Chakraborty, “Microscopic origin of frictional rheology in dense suspensions: correlations in force space,” *arXiv preprint arXiv:1804.03155* (2018).